energies

MDPI

Article

Numerical Characterization of an Ultrasonic Mist Generator as an Evaporative Cooler

Javier Ruiz *,†, Pedro Martínez †, Íñigo Martín † and Manuel Lucas

Department of Mechanical Engineering and Energy, Universidad Miguel Hernández, Avda. de la Universidad, s/n, 03202 Elche, Spain; pedro.martinez@umh.es (P.M.); inigo.martin@alu.umh.es (Í.M.); mlucas@umh.es (M.L.)

* Correspondence: j.ruiz@umh.es

† These authors contributed equally to this work.

Received: 30 April 2020; Accepted: 29 May 2020; Published: 9 June 2020

Abstract: Pre-cooling of inlet air using evaporative cooling is an effective approach to enhance the performance of air-cooled condensers in air conditioning applications. Ultrasonic mist generators have emerged as a promising alternative to conventional evaporative cooling systems based on cooling pads or spray cooling. This paper presents the developed numerical model of an ultrasonic mist generator for the evaporative pre-cooling of the inlet air of the condenser in air conditioning applications. The model was validated against the experimental data obtained in a wind tunnel experimental facility. A parametric analysis including some physical variables involved in the cooling process was carried out, including the main axial air velocity, the injection air velocity and the water mass flow rate of atomized water. The dimensionless groups water-to-air mass flow and air-to-air mass flow ratios were found to most affect the average evaporative cooling efficiency. A maximum value of 0.654 was found for the studied conditions. The optimization analysis carried out shows that the operational ranges leading to the best overall performance are $5 \times 10^{-4} \leq \dot{m}_w/\dot{m}_{a_T} \leq 0.002$ and $0.035 \leq \dot{m}_{a_i}/\dot{m}_{a_T} \leq 0.05$. Under these conditions, there is a better distribution of the water mist throughout the control section and a more homogeneous and effective evaporative cooling process.

Keywords: evaporative cooling; ultrasonic nebulizer; cooling efficiency; CFD

1. Introduction

The energy consumption used in buildings around the world today in air conditioning systems or electric fans to stay cool accounts for almost 20% of their total electricity consumption. This trend mainly grows due to the demographic and economic development of the countries with warmer climates. Wider access to refrigeration is beneficial to human development, economic productivity, health and well-being. However, this further development will have implications for countries' overall energy demand, putting pressure on electricity grids and increasing local and global emissions [1]. An answer to achieve a more sustainable path necessarily involves the use of renewable energy and the use of very efficient technologies.

Evaporative cooling techniques applied to the condenser of a refrigerating machine represent one of the most effective and immediately applicable solutions for improving the efficiency of domestic and commercial air conditioning systems worldwide. With these techniques, it is possible to reduce significantly, mainly in countries with hot-dry climates, the energy demand and the high consumption peaks. A considerable amount of studies in the literature show the benefits of pre-cooling techniques, applied to different air conditioning systems. There are different strategies to reduce the temperature of the air entering the condenser. The most widely studied systems can be classified into: evaporative packings or pads and spray or mist generators. For direct evaporative coolers, Martínez et al. [2] studied the influence of evaporative pad thickness on the energy consumption of a split-type air

conditioner. The experimental data show that for a pad thickness of 100 mm an improvement of 10.6% in the overall coefficient of performance (COP) was achieved. Ibrahim et al. [3] proposed using condensate to pre-cool condenser air for a split-type air-conditioner. With a reduction in the temperature of the air entering the condenser of approximately 4 °C, an increase of COP by 21.4% with an enhanced cooling capacity was obtained. The main drawback of pre-cooling systems based on evaporative pads is the additional pressure drop produced in the condenser air stream. Furthermore, this effect is present even if pre-cooling is not activated.

Mist or deluge systems give further flexibility for installation due to their low profile piping network and provide negligible flow resistance to the air stream, compared with direct evaporative coolers. Yu et al. [4] experimentally studied the cooling effectiveness of mist in pre-cooling condenser air for an air-cooled chiller. The chiller had a capacity of 282 kW and operated with a mist system under dual modes: conventional head pressure control (normal mode) and variable speed control for condenser fans (VSD mode). In a subtropical climate, pre-cooling the condenser air by mist brought an increase of 0.36–8.86% and 0.34–10.19% in the coefficient of performance of the chiller under the normal mode and the VSD mode, respectively. However, the use of water spray or deluge, if water droplets are carried by the airstream to the heat exchanger bundles of the condenser, can cause fouling, scaling and/or corrosion on the heat exchanger bundles. However, these problems can be avoided if all the droplets evaporate completely before reaching the heat exchanger.Special spray nozzles or wet media may be required to meet the requirement. High-pressure nozzles provide small water droplets but at a higher cost [5]. In view of the drawbacks found in current techniques for pre-cooling, a search for alternatives seems appropriate.

Applications of ultrasonic energy to enhance a wide variety of processes or to improve system efficiency have been explored in recent years. Yao [6] made an overview of studies about the applications of ultrasound as a new technology in the field of Heating, Ventilation and Air-Conditioning (HVAC). They claimed that, from a general point of view, all the effects produced by ultrasound could be interesting in applications involving heat or mass transport, decreasing both the external and internal resistance to transport. Recently, Yao et al. [7] presented a review of the state-of-the-art of high-intensity ultrasound and its applications. Regarding heat transfer enhancement in liquid environment, they found that ultrasound not only increased heat transfer rates, but might also be a solution to fouling reduction. In relation to droplet atomization. They explained the ultrasonic atomization by the surface-wave theory and the cavitation theory. The authors did not specifically cite evaporative cooling as an application of ultrasound, denoting the little attention it has received to date.

Computational Fluid Dynamics (CFD) techniques have been used extensively in recent decades as an effective and powerful tool capable of characterizing spray cooling in different applications. CFD enables scientists and designers to understand the physical principles of spraying processes saving time and effort in tedious experimental work. Literature review shows that several authors face the analysis of spray cooling for different applications using CFD models. Tissot et al. [8] used an Eulerian–Lagrangian model to simulate droplet motion in an air flow was used. They investigated the droplet evaporation for various loadings, spray characteristics and injection solutions on a small channel that was related to a real condenser. They concluded that there must be a compromise between the size of the water droplets and the injection area for optimal cooling. Hou et al. [9] simulated the characteristics of multi-nozzles arrangements for spray cooling. They examined the effects of nozzle inlet pressure, mass flux, nozzle-to-surface distance and nozzle numbers on the droplet Sauter Mean Diameter (SMD or d_{32}). Alkhedhair et al. [10] numerically investigated the droplet transport, the droplet evaporation and the resulting cooling of the inlet air pre-cooling with water sprays to enhance the performance in natural draft dry cooling towers for a range of conditions and a number of spray nozzle characteristics. They paid special attention to the droplet size requirements to achieve full evaporation. They reported a significant improvement in cooling performance: average temperature reduction of 8.1 °C in the droplet saturated region and 4.8 °C across the domain were attained. Xia et al. [11] conducted CFD analysis of a wind tunnel with a spray cooling in vertical arranged

nozzle (VAN) and in horizontal arranged nozzle (HAN). They used the geometric dimensions of the natural draft dry cooling tower built at the University of Queensland (Australia) as a reference. They concluded that a vertical arrangement has the best performance, with a pre-cooling of 4.1–7.2 °C under complete evaporation. Sadafi et al. [12] showed the possibility of using saline water for pre-cooling the inlet air to a heat exchanger. They developed a CFD model to predict the wet length of saline water droplets in spray cooling for different ambient conditions and spray characteristics. They validated the model by using their own experimental data conducted in a wind tunnel. A dimensionless correlation for wet length in horizontal flow is presented. Few references have been found in the bibliographic review related to the numerical simulation of ultrasonic mist generators, and none of them was related to the evaporative pre-cooling of the inlet air of the condenser in air conditioning applications. Recently, Kim et al. [13] numerically simulated an ultrasonic gas atomizer. Through numerical simulation, they decided generation position and operating conditions of ultrasound atomizer.

The literature review revealed that ultrasound is a promising method to improve the design of evaporative pre-cooling systems. Ultrasonic mist generators eliminate pressure loss at the inlet air stream to the condenser and allow controlling the characteristics of the generation of the atomization.

The main objective of this study was to develop a numerical model of an ultrasonic mist generator. The model was validated using the results obtained in several experimental test runs conducted for this purpose. Afterwards, secondary objectives consisted of conducting a parametric analysis including some physical variables involved in the cooling process, and, finally, carrying out an optimization process regarding the overall cooling performance, for the above mentioned application, of the ultrasonic generator.

The experimental setup and the description of the CFD model is presented in Section 2. Then, the results predicted by the CFD model (validation, parametric analysis and optimization) on the evaporative cooling are presented in Section 3. Finally, the most important findings of this research are summarized in Section 4.

2. Materials and Methods

2.1. Experimental Test Facility

To evaluate the performance and cooling capacity of the water mist produced by the ultrasonic mist generator, a set of tests were carried out in an experimental test facility specifically adapted for this purpose. The test rig mainly consists of two components: an ultrasonic mist generator unit and a subsonic wind tunnel.

The ultrasonic mist generator consists of a compact mist maker device equipped with 10 ultrasonic transducers, immersed in a tank with a steady water level, where the water atomization process is properly controlled. The ultrasonic transducer is composed of a piezo-electric crystal coupled to a 16-mm diameter ceramic disc. When submerged in water, the transducer is capable of transforming high frequency electronic signals, typically ranging from 0.8 to 1.65 MHz, into high frequency mechanical oscillations on the disc. When the water attempts to follow the ceramic disc's movements, it is unable to keep up with the high-frequency oscillations. As a result, the water is detached from the disc on the negative oscillations and produces a transitory vacuum, where the water cavitates and changes into steam. Then, on the positive oscillation, the steam water is driven by the high pressure wave through the water surface. In this adiabatic process, a fine water mist is formed, with droplet diameters on the scale of a few tens of microns, which are easily incorporated into the air flow.

To control the amount of atomized water produced by the ultrasonic mist generator, it is possible to select the number of ultrasonic transducers operating simultaneously and also to regulate the rotation speed of a fan coupled to the tank. This fan generates the necessary positive pressure into the tank to drive the atomized water out of it. This speed control is carried out by using an Arduino UNO microcontroller board, programmed to make this adjustment by directly operating a potentiometer and displaying the updated rpm on the computer screen.

Table 1 shows the technical specifications and operating conditions of the mist maker unit while Figure 1 shows a schematic view of the components that compose the ultrasonic mist generator. The path of the secondary airflow through the nebulization chamber, which carries and injects the atomized water droplets into the main airstream, is also depicted.

Table 1. Technical specifications and operating conditions of the mist maker unit.

10 Head Ultrasonic Mist Maker	
Number of atomizing cores	10
Ceramic core diameter	16 mm
Input voltage	DC 48 V
Input power	20 W/core
Resonance frequency	1650 ± 50 kHz
Maximum atomization amount	2.5 L h^{-1}
Working water temperature	1–55 °C
Working water level	60–80 mm

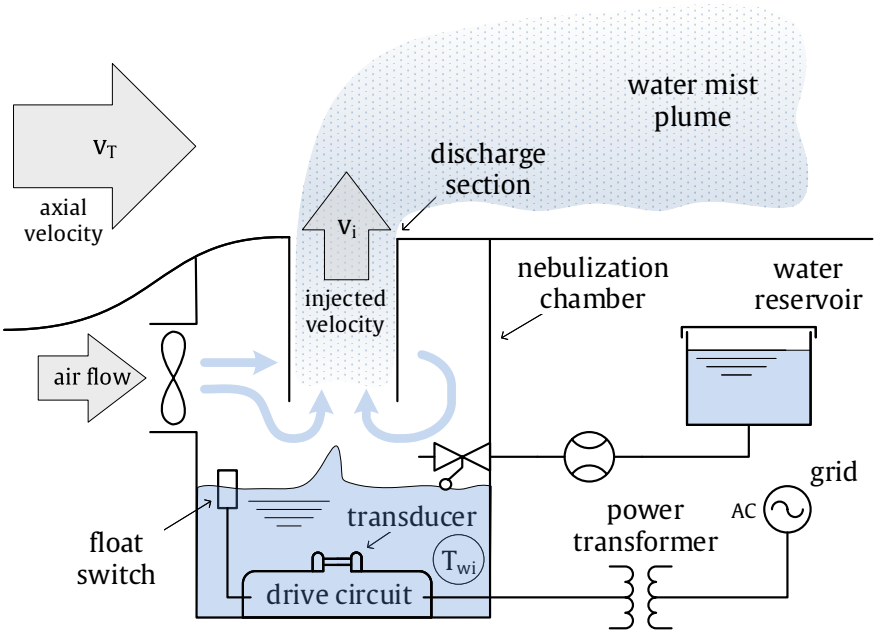

Figure 1. Schematic view of the principal components that make up the ultrasonic mist generator and layout of the two flows considered in the numerical model.

The open-circuit, subsonic wind tunnel shown in Figure 2 was used to perform the ultrasound evaporative cooling experimental tests. The nozzle along the honeycomb baffle (anti-turbulence screen) adapted in the entrance (leftmost part of the tunnel) ensures the uniform, stable velocity profiles of the air flow. The test section of the wind-tunnel is 5.3 m long with a cross section of 0.492 × 0.712 m^2, while the nozzle dimensions are 1.2 × 1.7 m^2 (cross-sectional area) and a length of 1.55 m.

The induced draft airflow rate is driven by a 0.55-kW axial fan located at the exit of the tunnel, and was maintained at different levels by a variable-frequency drive. It allows to set different air flow speeds in the tunnel, ranging 0–3 m s^{-1}. This results in a maximum available volumetric air flow rate of 3783 m^3 h^{-1}. A full description of the experimental test facility (wind tunnel) can be found in [14–16].

Figure 2. Subsonic wind tunnel facility employed in the experimental tests: (**a**) subsonic wind tunnel; (**b**) test section; (**c**) nozzle; (**d**) diffuser; (**e**) data acquisition system; (**f**) ultrasonic mist generator; and (**g**) structure of water mist stream.

2.2. Wind-Tunnel Experiments

A series of tests were conducted to assess the cooling performance of the mist generator unit and validate the numerical model. Table 2 summarizes the main characteristics of the validation tests measured by the sensors installed on the test rig.

Table 2. Summary of the experimental tests carried out.

v_T (m s^{-1})	v_i (m s^{-1})	$\dot{m}_w$ (kg s^{-1})	T_∞ (°C)	ϕ_∞ (%)	T_1 (°C)	ϕ_1 (%)	T_2 (°C)	ϕ_2 (%)	T_3 (°C)	ϕ_3 (%)
1.615	3.315	2.828×10^{-4}	25.43	51.78	21.63	81.97	25.62	50.61	25.90	49.75
0.512	2.994	2.433×10^{-4}	24.23	55.28	21.93	73.09	22.40	68.67	24.89	53.05
2.183	3.450	2.997×10^{-4}	25.73	49.78	22.51	72.25	25.95	49.08	26.05	48.81
0.508	4.152	3.864×10^{-4}	24.43	54.28	21.93	73.09	20.67	83.48	22.58	67.82
1.095	3.023	2.468×10^{-4}	25.23	52.08	21.65	81.41	25.39	50.88	25.67	49.88

The inlet (ambient, T_∞) air dry-bulb temperature and relative humidity (ϕ_∞) were measured by using a meteorological station placed in the vicinity of the wind tunnel. An array of three thermo-hygrometers were used to register the temperature and relative humidity vertical distributions (T_1, T_2, T_3, ϕ_1, ϕ_2 and ϕ_3). They were located at the control section, 1500 mm downstream from the

sprayed mist discharge section. A hot-wire anemometer, placed 435 mm upstream from the control section, was employed to measure the averaged air flow velocity in the wind tunnel, v_T. As discussed in [14], the nozzle ensures a uniform velocity profile in the test section of the wind tunnel. Hence, this measurement suffices to obtain the mean velocity and the volumetric flowrate. The injection velocity of the sprayed mist discharge section, v_i, was registered by an impeller anemometer located at the nebulization chamber. All measurements were recorded with a Keysight 34970A data acquisition unit. A schematic arrangement of the measurement set-up is shown in Figure 3.

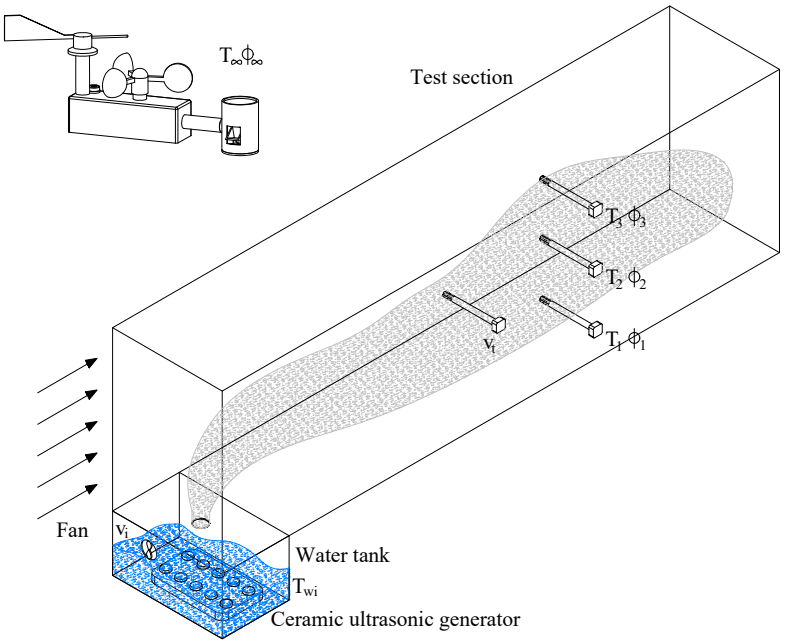

Figure 3. Schematic arrangement of the test section, mist generator and measurement devices.

A gravimetric method was used to determine the injected mass flowrate of water. It consisted of measuring the weight of the water supplied to the mist generator in a known time interval by weighting the make-up water reservoir.

Finally, the droplet size distribution concerning the ensemble of water droplets generated by the mist generator was determined in order to define the appropriate boundary condition for the CFD model. A photographic technique was the method employed to determine the droplet distribution characteristics. This method consisted of directly photographing the droplets by a high resolution camera. An auto flash unit was used to freeze the droplet movement as they were ejected from the discharge section. The photographs were taken by arranging the flash on the opposite side of the camera position and using a remote trigger, while keeping the water mist flowing between the two devices. The photos taken with the camera have a native resolution of 7360 $\times$ 4912 pixels and were processed with a graphics editing software to increase contrast and acutance. A subsequent image analysis technique was employed to measure the droplet size using the ImageJ and Fiji software. To estimate the droplet diameter, the two-dimensional circular area registered in the photographs and a sphericity filter ranging from 0.8 to 1 were used to minimize the measuring error. Figure 4 gives an example of high-speed photography, where the movement of the droplets is captured to determine their diameter and size distribution using digital image processing.

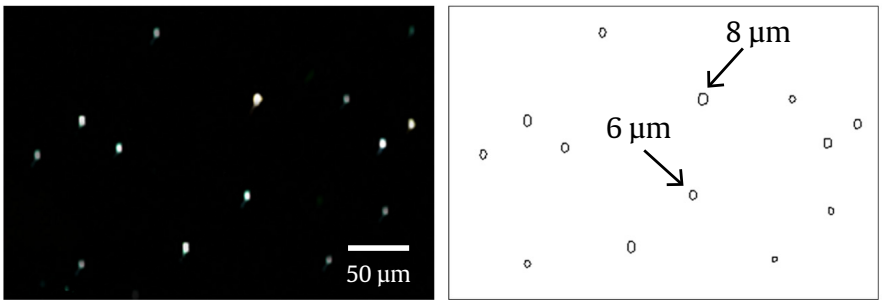

Figure 4. Example of high-speed photography showing diameter and size distribution of the droplets.

Figure 5 depicts the results of the droplet distribution generated by the ultrasonic generator. Figure 5a shows the histogram. As can be seen, the diameters mostly range from 1 to 25 µm, although some droplets up to 40 µm are observed. The arithmetic mean diameter of the droplets produced by the mist generator under the testing conditions is approximately $d_{10} = 8.1$ µm and the calculated Sauter mean diameter $d_{32} = 13.2$ µm. Both of them were calculated according to the general mean diameter expression shown in Equation (1).

$$d_{pq} = \left[\frac{\sum_{i=1}^{N} n_i d_{d,i}^{p}}{\sum_{i=1}^{N} n_i d_{d,i}^{q}} \right]^{\left(\frac{1}{p-q}\right)} \tag{1}$$

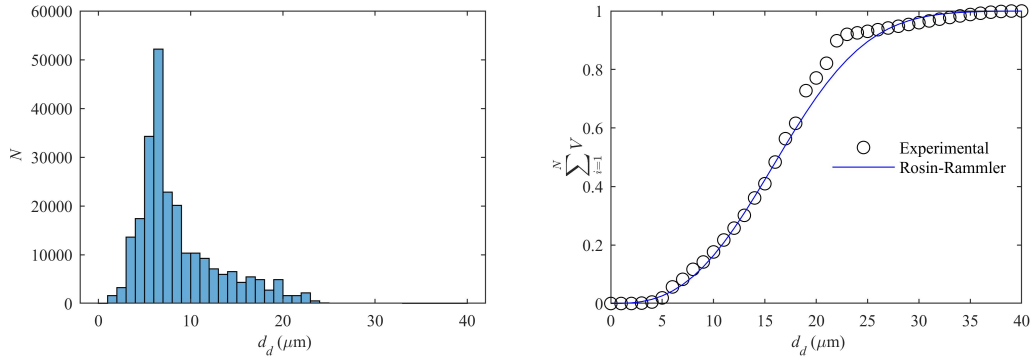

Figure 5. Experimental droplet distribution results: (**a**) histogram; and (**b**) cumulative mass distribution and Rosin–Rammler fit (Equation (2)).

The Rosin–Rammler distribution function was used to fit the experimental data of the drops emitted from the ultrasonic generator. The Rosin–Rammler function is an empirical relation used to correlate measured cumulative mass distribution data. This function has been used by many authors [17,18] to fit the experimental data of an ensemble of droplets. It can be expressed as,

$$M = 1 - e^{-\left(\frac{d_d}{\bar{d}}\right)^n} \tag{2}$$

where M is the cumulative mass fraction; $\bar{d}$ is the Rosin–Rammler mean drop diameter, which is obtained from the measured cumulative mass distribution at the diameter where the cumulative mass distribution is $1 - e^{-1}$; and the shape factor, n, can be determined by an average of Equation (3) for each drop diameter interval.

$$n = \frac{\ln(\ln M)}{\ln\left(\frac{d_d}{\bar{d}}\right)} \tag{3}$$

Figure 5b illustrates the experimental cumulative mass distribution, which is a distribution curve that gives measured cumulative mass fraction data as a function of drop diameters. The cumulative mass fraction at a certain drop diameter is defined as the drop mass fraction of which the drop diameters are smaller than that specific diameter. The Rosin–Rammler fit (Equation (2)) is presented along the experimental data. The fitting coefficients for Equation (2) correspond to $\bar{d} = 18.6$ μm and $n = 2.76$.

2.3. Physical Model

The physical domain considered in the simulations reproduces a portion of the experimental facility where the tests were performed (Section 2.1). It consists of a 2.5 m long, 0.492 m wide and 0.712 m high ($L \times b \times h$) domain (Figure 6). Spray injection was placed at a circular-shaped inlet section ($D = 56$ mm diameter) located on the tunnel floor and $l = 0.15$ m from the inlet and directed vertically in a cross-current direction with the airflow.

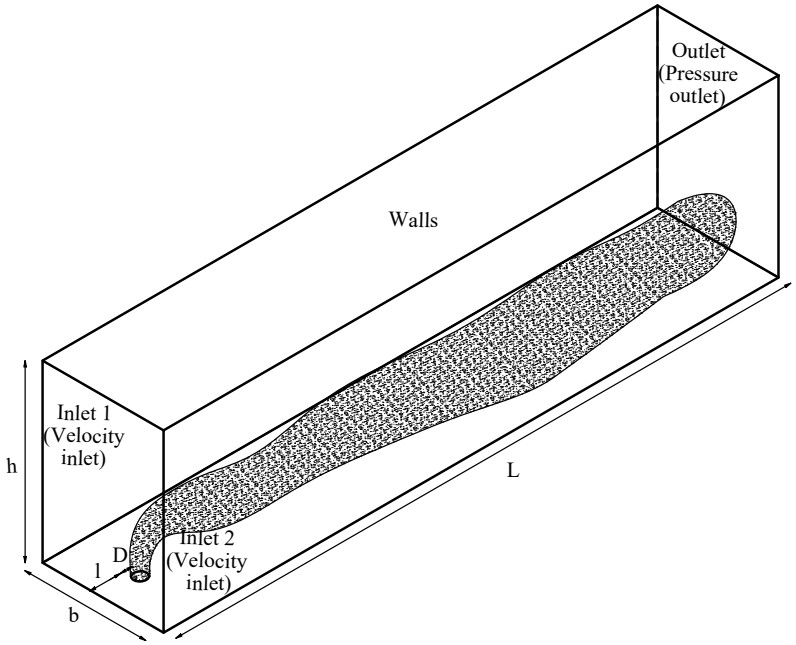

Figure 6. Wind tunnel domain considered in the simulations and boundary conditions.

2.4. Mathematical Method (Governing Equations)

2.4.1. Continuous Phase (Moist Air)

The airflow was assumed to be steady, incompressible and turbulent flow. The Reynolds-Averaged Navier–Stokes equations (RANS) were used along the standard k-ϵ turbulence model. No turbulence model can be considered superior to the others [19], but the standard k-ϵ turbulence model has been reported to accurately predict the flow field and droplet evaporation in several spray cooling applications [10,20–22]. The influence of water droplets on the airflow was considered by introducing the source terms of mass, momentum and energy into the air-side governing equations.

In spray cooling applications, heat, mass and momentum is transferred between the moist, unsaturated air stream and the water droplets. Processes related to heat-and-mass transfer between different phases are governed by mass, momentum, energy and species conservation principles. This multiphase flow is described by the set of equations that governs the continuous phase (internal moist air inside the wind tunnel) and the set of equations for the discrete phase (ultrasound-generated

water droplets). The continuous and discrete phase equations are coupled by the source terms of the conservation equations. In this study, an Eulerian–Lagrangian approach was used.

$$\frac{\partial(\rho v_i)}{\partial x_j} = S_m \quad (4)$$

$$\frac{\partial(\rho v_i v_j)}{\partial x_j} = -\frac{\partial p}{\partial x_i} + \frac{\partial \tau_{ij}}{\partial x_j} + \rho g_i + S_{mo} \quad (5)$$

$$\rho v_i \frac{\partial e}{\partial x_j} = -p\frac{\partial v_i}{\partial x_j} + \frac{\partial}{\partial x_j}\left(k\frac{\partial T}{\partial x_j}\right) + \frac{\partial}{\partial x_j}\left(\sum_{i'=1}^{n} h_{i'} J_{i'}\right) + \phi_v + S_e \quad (6)$$

$$\rho v_i \frac{\partial m_j}{\partial x_j} = -\frac{\partial J_{i',i}}{\partial x_j} + S_m \quad (7)$$

$$J_{i',i} = -\rho D_{f_{i',m}} \frac{\partial m_j}{\partial x_j} \quad (8)$$

Here, S_m, S_{mo} and S_e represent the mass, momentum and energy source terms introduced by water droplets, respectively, and $J_{i',i}$ is the diffusion flux of species i'.

2.4.2. Discrete Phase

The equations for the spherical water droplets are written in a Lagrangian reference frame. The trajectory of a discrete phase particle is obtained by integrating the force balance on the droplet (Newton's second law of motion),

$$\frac{dv_d}{dt} = \frac{18\mu}{\rho_d d_d^2}\frac{C_D \,\mathrm{Re}}{24}(v - v_d) + g\frac{\rho_d - \rho}{\rho_d} \quad (9)$$

$$\frac{dr_d}{dt} = v_d \quad (10)$$

The drag coefficient (C_D) included in the the drag per unit droplet mass term can be calculated as reported by Morsi and Alexander [23].

Due to the existence of a temperature difference and a vapor concentration gradient between the water droplets and the unsaturated air, heat and mass transfer between them occur. The energy conservation equation of a droplet, neglecting the radiation effect, is expressed as,

$$m_d c_p \frac{dT_d}{dt} = h_C A_d (T - T_d) + \frac{dm_d}{dt} h_{fg} \quad (11)$$

It relates the temperature change in the droplet to the convective and latent heat transfer between the droplet and the continuous phase. The rate of evaporation of water changes according to,

$$\frac{dm_d}{dt} = h_D A_d M (y_s - y) = h_D A_d (\rho_s - \rho) \quad (12)$$

The convective and mass transfer coefficients (h_C, h_D) are calculated from the Nusselt and Sherwood number correlations reported in [24,25],

$$\mathrm{Nu} = \frac{h_C d_d}{k} = 2 + 0.6\,\mathrm{Re}_d^{1/2}\,\mathrm{Pr}^{1/2} \quad (13)$$

$$\mathrm{Sh} = \frac{h_D d_d}{D_f} = 2 + 0.6\,\mathrm{Re}_d^{1/2}\,\mathrm{Sc}^{1/2} \quad (14)$$

2.5. Numerical Method

The boundary conditions employed in the present analysis are shown in Figure 6. Air enters the computational domain at the leftmost surface shown in the figure and at the circular-shaped inlet section placed at the bottom (mist discharge area). At both inlets, a uniform inlet air velocity boundary condition is specified, matching the experimental measurements. The air velocities range from 0.51 to 2.18 m s^{-1} and 2.99 to 4.15 m s^{-1} for both inlets. The flow Reynolds number is in the range of 15,865–86,892. A turbulence intensity of 5% was assumed for the inlet flows [26]. The incoming sprayed water was set to match experimental conditions. The injection velocity matched the continuous phase velocity and the droplets' temperature was set equal to the measured tap water temperature. The pressure was stated to be equal to the ambient pressure at the outlet section (pressure outlet). Wall boundary condition was selected for the tunnel walls. The zero heat flux and no-slip condition were imposed on them. The 'escape' boundary condition was set, meaning that the droplets exit the computational domain when they reach the walls or the tunnel exit [10]. The Rosin–Rammler distribution was employed to represent the measured droplet size distribution in the experiments.

The commercial code ANSYS FLUENT (version 19.1) [27] was utilized to numerically solve the governing equations. A grid independence study was conducted to ensure the accuracy of the numerical results. The Grid Convergence Index (GCI) method first reported by [28] was employed. The GCI is a measure of the percentage the computed value is away from the value of the asymptotic numerical value. In other words, it indicates an error band on how far the solution is from the asymptotic value. It can be calculated as,

$$\mathrm{GCI} = \frac{F_c|\varepsilon|}{r^s - 1} \tag{15}$$

Three different grids were considered in the analysis. All of them were generated with ANSYS MESHING. The GCI was computed for the predicted temperatures and the absolute humidities at the measuring plane (3 points). The maximum GCI in the fine-grid solution for these magnitudes is 0.06%. This small value for GCI shows a negligible dependence of the results on the grid size. The selected grid is an unstructured grid with 1,612,376 polyhedral cells and grid was retained for further analysis. The SIMPLE algorithm was employed to solve the coupling between continuity and momentum equations through pressure. All calculations were performed using discretization providing second order accuracy. The convergence criterion in each case was $|\varphi(i+1) - \varphi(i)|/\varphi(i) < 10^{-4}$, where i denotes the iteration number and φ can stand for any of the dependent variables.

3. Results and Discussion

3.1. Problem Validation

This section presents the validation of the stated numerical model with the experimental results obtained in the wind tunnel facility (Section 2.1).

A comparison of the temperature and humidity distributions in the measurement section (array of sensors) for the first test run in Table 2 is presented in Figure 7. This comparison between experimental and predicted results shows a good agreement. Even though the measurements are made at three specific locations, the numerical model successfully predicts the plume evolution and, as a result, the temperature profiles.

The comparison between the predicted and observed results for the dry-bulb temperature and the water mass fraction (ω) for the five tests in Table 2 is displayed in Figure 8a,b, respectively. The results show a good agreement, within 10% for both dry-bulb temperature and mass fraction, for all five experimental tests and three measuring locations displayed in Table 2. The exact reasons for the deviations observed in some cases between the observed and predicted results for the T_3 measurements (uppermost measuring location) are not clear, but they are probably caused by a combination of limitations in the location of the measuring points and experimental uncertainties.

The average deviations are around ±1 °C and ±0.5 g_w/g_{ma}. The average differences between the numerical results and the five test runs of experiments carried out is below 5% on average for the dry-bulb temperature and the water mass fraction (4.9% and 4.35%, respectively). In light of the presented results, the model can be considered validated.

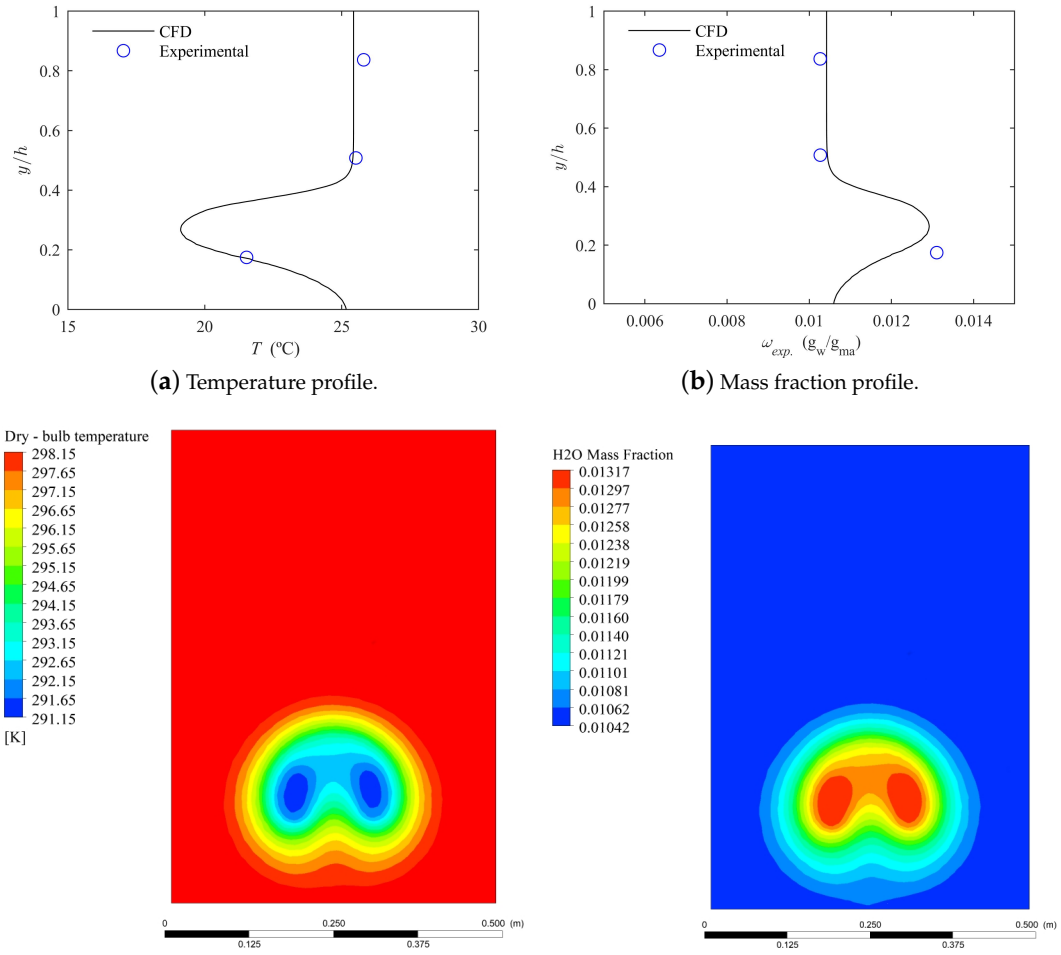

(**a**) Temperature profile. (**b**) Mass fraction profile.

(**c**) Temperature contour. (**d**) Mass fraction contour.

Figure 7. Comparison between predicted and experimental results (temperature and water mass fraction) evaluated at the measuring section for the first test presented in Table 2.

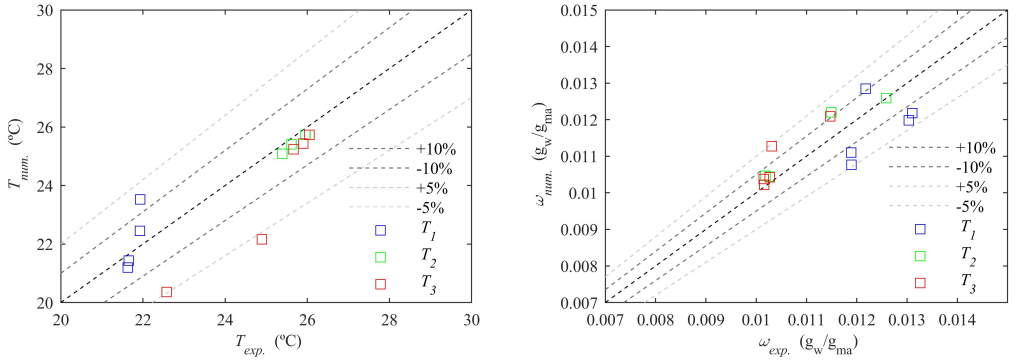

(**a**) Dry-bulb temperature. (**b**) Water mass fraction.

Figure 8. Comparison of calculated (CFD) and measured for the experimental tests displayed in Table 2.

3.2. Parametric Analysis

A parametric study was conducted to analyze the influence of some operating variables in the evaporative performance of the ultrasonic generator. The variables included in this study were the controllable variables that were thought to affect the most the performance of the evaporative cooler: average air flow axial velocity, injection velocity and mass flowrate of injected water. The selection of these magnitudes was justified because of the difficulty to study them independently with an experimental approach. This analysis can only be performed by means of a CFD simulation. In practical cases of pre-cooling of the incoming air flow in low to medium power range air-cooled condensers, the average air flow velocity through the condenser is usually in the range of 0.5–2.5 m s^{-1}, and most commonly 1–1.5 m s^{-1}. Accordingly, three levels of axial velocity were considered: 0.5, 1.5 and 2.5 m s^{-1}. Three additional levels of injected velocity (velocity at the outlet section of the sprayed mist discharge section) were set. They were selected for each specific mean axial velocity with the purpose of uniformly distribute the plume of water mist along the entire section of the tunnel. A uniform distribution of the plume is desirable in the evaporative pre-cooling process to achieve a homogeneous cooling of the air flow and a rapid evaporation of all the water droplets before they reach the air-cooled condenser. Hence, their values were different for each axial velocity, but mostly ranged 2.5–6 m s^{-1}. Finally, the water mass flowrate of water was selected specifically for each combination of air velocities aiming to set a maximum value for which the complete saturation of the plume was achieved. Again, three sets of mass flowrates values were defined for each combination ($5 \times 10^{-5} \leq \dot{m}_w \leq 1.2 \times 10^{-3}$kg s^{-1}). The total number of conducted simulations was equal to 27. The rest of the variables involved in the parametric analysis were considered constant with values similar than the ones registered during the experimental tests ($T_\infty = 25$ °C, $\phi_\infty = 0.5$ and $T_w = 25$ °C, $d_d = 35$ μm).

The evaporative cooling efficiency at the certain section, $\bar{\eta}^x$, is defined as the ratio of the mean temperature difference calculated at the evaluated section, $T_\infty - \bar{T}^x$, to the wet bulb depression ($T_\infty - T_{wb_\infty}$).

$$\bar{\eta}^x = \frac{T_\infty - \bar{T}^x}{T_\infty - T_{wb_\infty}} \tag{16}$$

Figure 9 shows the evaporative cooling efficiency evaluated at the outlet section of the domain, $\bar{\eta}^L$, as a function of the water-to-air (axial flow) mass flow ratio, $\dot{m}_w / \dot{m}_{a_T}$ for all the simulations conducted. The different series have been plotted using the same color for the axial velocity levels and the same symbol for the same injection velocity levels. The injection velocity levels do not match for each mean axial velocity level. This statement refers to the relative levels, 1, 2 and 3 for each of the mean axial velocity levels. For example, discharge velocity levels match for the first and second levels of axial velocity, being 2.5, 3 and 3.5 m s^{-1}. However, for the third level of axial velocity in the domain (2.5 m s^{-1}), the discharge velocities are 4, 5 and 6 m s^{-1}. As can be seen, the results are scattered over a wide range: from $\bar{\eta}^L = 0.026$ to 0.654. The maximum efficiency is $\bar{\eta}^L = 0.654$, observed for the case with the lowest mean axial velocity level (0.5 m s^{-1}), and highest injection air velocity and water mass flowrate (0.5 m s^{-1} and $\dot{m}_w = 5 \times 10^{-4}$ kg s^{-1}). The lowest, $\bar{\eta}^L = 0.026$, is observed for the highest mean axial velocity level (2.5 m s^{-1}) and lowest injection air velocity and water mass flowrate (4 m s^{-1} and $\dot{m}_w = 10^{-4}$ kg s^{-1}).

The general trend observed is that the efficiency increases with the water-to-air mass flow ratio, and with the air-to-air mass flow ratio, $\dot{m}_{a_i} / \dot{m}_{a_T}$, dimensionless form of the injection velocity at the sprayed mist discharge section. This can be justified as follows. As expected, by injecting a higher mass flow rate of water for the same mass flow rate of air (axial), the evaporation is favored. From the results predicted for the higher levels of mean axial velocity (green and red series in Figure 9), it can be guessed that this relationship is asymptotic, and there is a maximum amount of sprayed water that can exchange heat and mass with the air until it achieves full evaporation. On the other hand, a higher

injection velocity for a given axial velocity results in a water mist plume distributed more evenly over the domain cross-sectional area, increasing the overall evaporative efficiency.

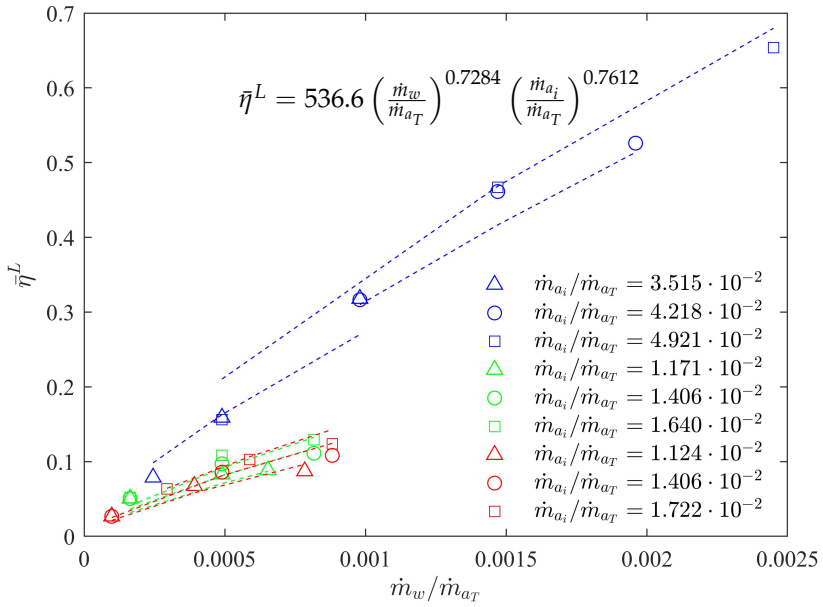

Figure 9. Evaporative cooling efficiency as a function of the water-to-air mass flow ratio for all the simulations conducted.

The general correlation displayed in Equation (17) fits the numerical data obtained in this study.

$$\bar{\eta}^L = a \left(\frac{\dot{m}_w}{\dot{m}_{a_T}}\right)^b \left(\frac{\dot{m}_{a_i}}{\dot{m}_{a_T}}\right)^c \tag{17}$$

The fitting coefficients were found to be $a = 536.6$, $b = 0.7284$ and $c = 0.7612$. The obtained correlation is specific for this application and valid for the ranges: $0.5 \leq v_T \leq 2.5$ m s^{-1}, $2.5 \leq v_i \leq 6$ m s^{-1} and $5 \times 10^{-5} \leq \times m_w \leq 1.2 \times 10^{-3}$ kg s^{-1}. The correlation reflects the trends discussed above. The signs of the coefficients are consistent with the observed variations of the parameters. The goodness of the fits was assessed by plotting them alongside the results in Figure 9 ($R^2 = 0.9835$). It was developed using regression method and the fitting coefficients were determined with 95% confidence bounds.

The evaporative cooling efficiency gives an overall representation of the cooling processes taken place in the domain since is referred to the mean temperature. However, this magnitude fails to represent local effects. For instance, there are areas where the air is cooled below the mean temperature stated by the evaporative cooling efficiency. To perform a quantitative comparison between the studied cases, the percentage area at a certain temperature was defined (A_T^x). It represents the portion of the total cross-sectional area of the tunnel where the temperature is smaller than that specific temperature. For example, $A^L_{25°C} = 1$ means that all the area at the domain outlet ($x = L$) is below 25 °C.

Figure 10 depicts the variation of A_T^L as a function of the air temperature for three representative cases. With the purpose of describing the results related to this magnitude, the following nomenclature has been adopted. A concave-shaped curve is defined whenever A_T^L dramatically drops for relatively high air temperatures, ~25 °C (note that $T_\infty = 25$°C). This means that the cooled area is concentrated into a small portion of the total cross-sectional area. As shown in Figure 10, the green and red series, corresponding to the higher levels of the mean axial velocity in the domain (1.5 and 2.5 m s^{-1}), fall into this category. In all of these cases, the portion of the total cross-sectional area of the tunnel where the temperature is smaller than 25 °C is around 40% at the most.

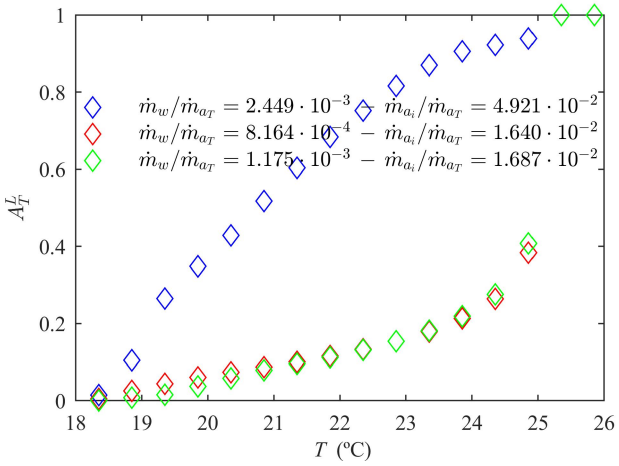

Figure 10. Variation of A_T^L as a function of the air temperature for three representative cases.

On the other hand, a convex-shaped curve represents a smoother, less steep transition for A_T^L with the temperature. The curve presented corresponds to the lowest level of the mean axial velocity in the domain (0.5 m s^{-1}) and the highest v_i and $\dot{m}_w$ levels. In these cases, A_T^L values around 50% correspond to temperature drops ranging 1–4 °C. Some cases present relatively big areas (∼20%) of temperatures close to T_∞ (temperature drop around 5 °C). This behavior can be explained because of the relative contributions of the inlet air streams: axial and sprayed mist discharge section. If the velocity in the axial direction of the domain is dominant with respect to the injection velocity, the sprayed water mist is dragged by the air flow velocity and the atomized droplets are concentrated in a small area. This region is obviously rapidly cooled due to the evaporation of the droplets, but avoids the energy transport to other sections of the domain. These phenomena are illustrated in Figure 11. Here, the comparison between the best ($v_T = 0.5$ m s^{-1}, $v_i = 3.5$ m s^{-1} and $\dot{m}_w = 5 \times 10^{-5}$ kg s^{-1}) and the worst ($v_T = 2.5$ m s^{-1}, $v_i = 2$ m s^{-1} and $\dot{m}_w = 4 \times 10^{-4}$ kg s^{-1}) cases attending to the variation of A_T^L with the temperature is shown. Higher values of $\dot{m}_w/\dot{m}_{a_T}$ and $\dot{m}_{a_i}/\dot{m}_{a_T}$ produce a more homogeneous distribution of water mist, leading to lower average temperatures and better efficiencies. The optimal values of $\dot{m}_w/\dot{m}_{a_T}$ and $\dot{m}_{a_i}/\dot{m}_{a_T}$ in that regard are 2.5×10^{-3} and 0.025. Lower values of $\dot{m}_{a_i}/\dot{m}_{a_T}$ result in a smaller plume (characteristic dimension) that makes the evaporation process much more difficult and makes the droplet lifetime much longer.

The last indicator discussed in this section is the wet length, L_w. The wet length is the distance from the sprayed mist discharge section for which the water droplets fully evaporate. This phenomenon can cause corrosion, scaling and fouling on the heat exchanger bundles if not fully evaporated water droplets are carried out by the airstream to the heat exchanger bundles of the condenser.

The wet length (or its dimensionless form, L_w/L) is higher than the unity in almost all the cases simulated, meaning that some droplets exit the domain through the outlet section. In only a few cases, this dimensionless group is lower than 1. As expected, low values of $\dot{m}_w/\dot{m}_{a_T}$ and high values of $\dot{m}_{a_i}/\dot{m}_{a_T}$ promote the plume distribution over the section and, as a result, the evaporation.

Figure 12 depicts, as an example, prediction of the droplets' trajectories in two representative cases. Figure 12a depicts the results predicted for the case $v_T = 2.5$ m s^{-1}, $v_i = 5$ m s^{-1} and $\dot{m}_w = 9 \times 10^{-4}$ kg s^{-1} ($\dot{m}_w/\dot{m}_{a_T} = 8.164 \times 10^{-4}$ and $\dot{m}_{a_i}/\dot{m}_{a_T} = 1.640 \times 10^{-2}$). As can be seen, the majority of the droplets leave the domain before they evaporate. On the other hand, Figure 12b depicts the results predicted for the case $v_T = 0.5$ m s^{-1}, $v_i = 3.5$ m s^{-1} and $\dot{m}_w = 10^{-4}$ kg s^{-1} ($\dot{m}_w/\dot{m}_{a_T} = 4.899 \times 10^{-4}$ and $\dot{m}_{a_i}/\dot{m}_{a_T} = 4.921 \times 10^{-2}$).

The observations of this performance indicator can be employed to identify the ranges of $\dot{m}_w/\dot{m}_{a_T}$ and $\dot{m}_{a_i}/\dot{m}_{a_T}$ that produce a more homogeneous distribution of water mist and evaporation. The cases where the dimensionless wet length is lower than the unity is in the range

of $2.5 \times 10^{-4} \leq \dot{m}_w / \dot{m}_{a_T} \leq 10^{-3}$ and $0.035 \leq \dot{m}_{a_i} / \dot{m}_{a_T} \leq 0.05$. Accordingly, operating outside these ranges should be avoided to achieve a full evaporation of the sprayed water.

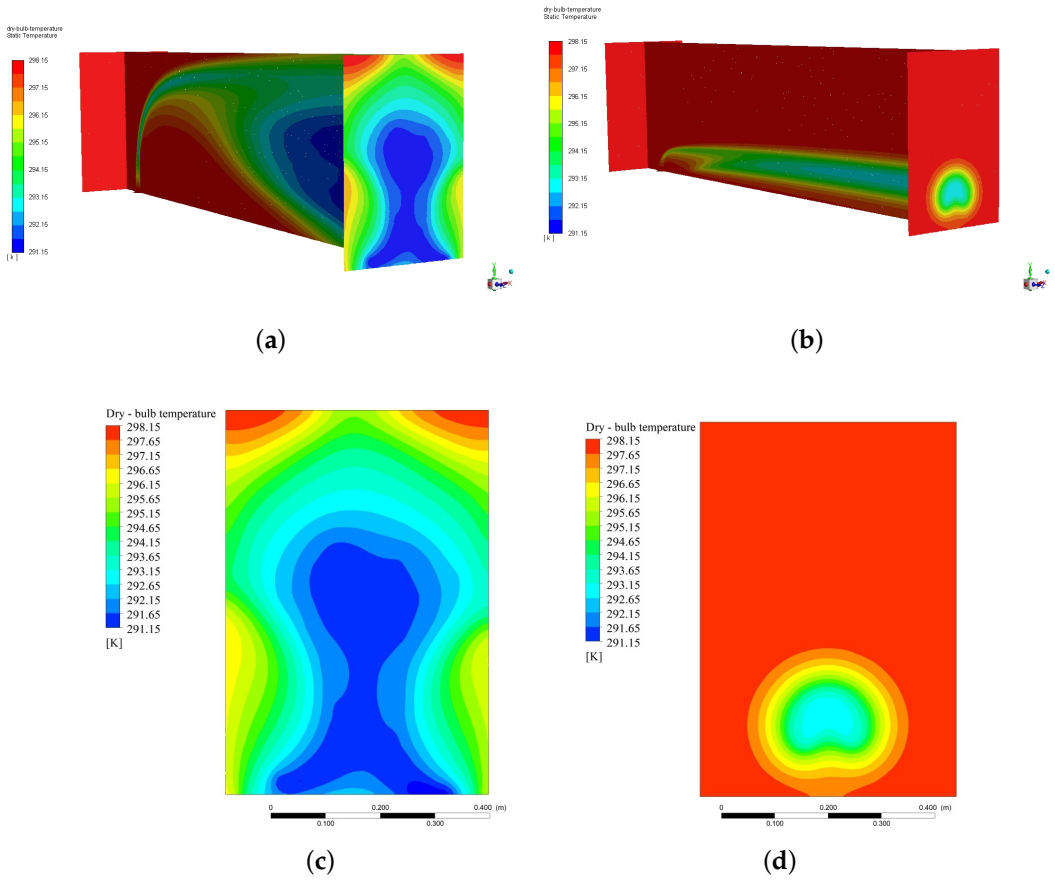

Figure 11. Temperature contours in the axial mid plane and the outlet section of the domain: (**a**,**c**) $v_T = 0.5$ m s^{-1}, $v_i = 3.5$ m s^{-1} and $\dot{m}_w = 5 \times 10^{-5}$ kg s^{-1}; and (**b**,**d**) $v_T = 2.5$ m s^{-1}, $v_i = 4$ m s^{-1} and $\dot{m}_w = 4 \times 10^{-4}$ kg s^{-1}.

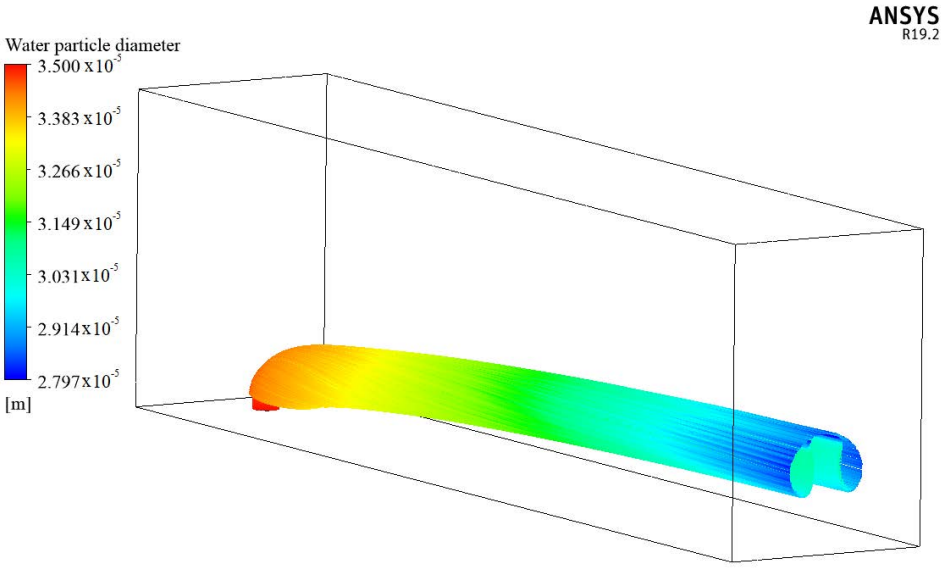

(**a**) Case $v_T = 2.5$ m s^{-1}, $v_i = 5$ m s^{-1} and $\dot{m}_w = 9 \times 10^{-4}$ kg s^{-1}.

Figure 12. *Cont.*

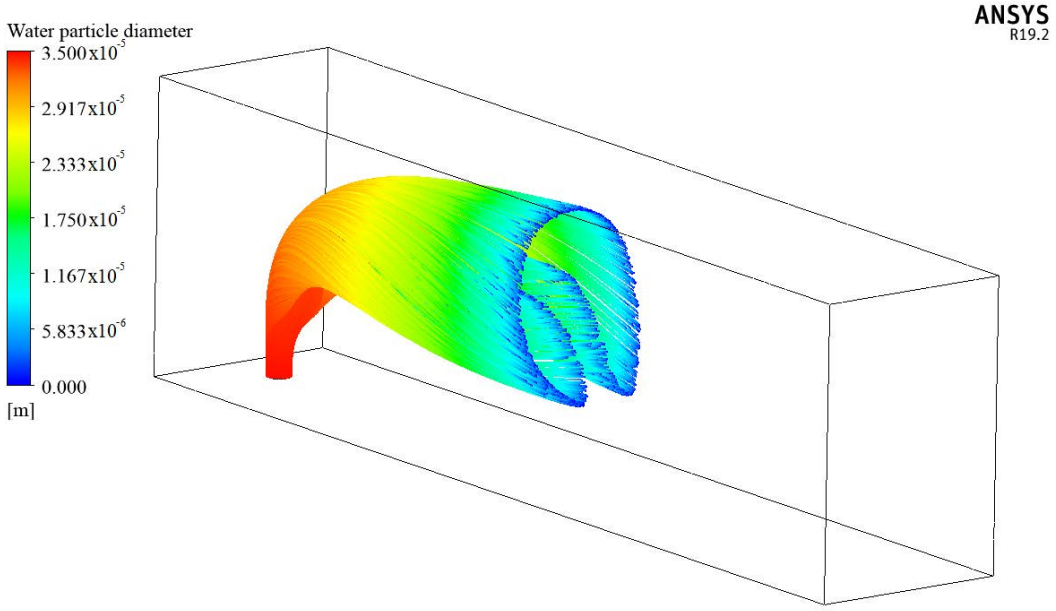

(**b**) Case $v_T = 0.5$ m s^{-1}, $v_i = 3.5$ m s^{-1} and $\dot{m}_w = 10^{-4}$ kg s^{-1}.

Figure 12. CFD prediction of the droplets' trajectories.

3.3. Optimization Analysis

From the above discussion, it has been highlighted that an increase of $\dot{m}_w$ increases the cooling efficiency, at least until the saturation is reached. However, that will involve an increased power consumption to drive the ultrasonic generator. Under these conditions, the cooling capacity, $\dot{Q}_{\text{cooling}}$, defined as in Equation (18), is also increased due to the temperature difference (via the cooling efficiency).

An increase of $\dot{m}_{a_T}$ leads to a lower evaporative efficiency and a higher consumption in the fans. Its effect on the cooling capacity is not straightforward since it is affected by opposing effects: $\uparrow \dot{m}_{a_T}$ and $\downarrow \Delta T$ (via the cooling efficiency).

$$\dot{Q}_{\text{cooling}} = \dot{m}_{a_T} c_{p_{ma}} \left(T_\infty - \bar{T}^L \right) \tag{18}$$

The relative contribution of all of these effects is included in the overall evaporative coefficient of performance (COP) (Equation (19)):

$$\text{COP} = \frac{\dot{Q}_{\text{cooling}}}{\dot{W}_{\text{fan}_T} + \dot{W}_{\text{fan}_i} + \dot{W}_{\text{ultrasound}}} \tag{19}$$

Therefore, this magnitude was selected as the key parameter to conduct an optimization analysis. The power consumption required by the fans was calculated by using the well-known fan performance equation (Equation (20)).

$$\eta_f = \frac{Q \Delta p}{\dot{W}_{\text{fan}}} \tag{20}$$

The electric power absorbed by the ultrasonic generator was estimated by calculating the number of transducers required to generate the injected mass flow rate of water. Then, this value was linked to the power consumption per transducer. At this stage, the measured values regarding the water generation and power consumption per transducer were used.

Figure 13 presents the variation of the coefficient of performance against the water-to-air mass flow ratio for different $\dot{m}_{a_i} / \dot{m}_{a_T}$ levels. The ultrasonic generator accounts for the major power consumption. Around 70–90% of the total consumption is used to drive the generator, while the remainder is mainly

absorbed by the secondary fan (sprayed mist discharge section). The theoretical power to generate the main airflow is almost negligible compared to the other power uses. Hence, the COP values are mainly affected by the ratio $\dot{m}_w/\dot{m}_{a_T}$. Generally speaking, the COP decreases with the increase of $\dot{m}_w/\dot{m}_{a_T}$. This is mainly due to the ultrasound power consumption. The maximum value for the COP is 7.01, which is attained by the combination $\dot{m}_w/\dot{m}_{a_T} = 9.8 \times 10^{-4}$ and $\dot{m}_{a_i}/\dot{m}_{a_T} = 0.0351$. The operation within the ranges $5 \times 10^{-4} \leq \dot{m}_w/\dot{m}_{a_T} \leq 0.002$ and $0.035 \leq \dot{m}_{a_i}/\dot{m}_{a_T} \leq 0.05$ guarantees a COP higher than 6. In this region, the trade-off of the above-mentioned trends concerning the cooling capacity along the power consumption is the best. These ranges also match the operational ranges leading to the best operation regarding the wet length. Therefore, the benefit is two-fold.

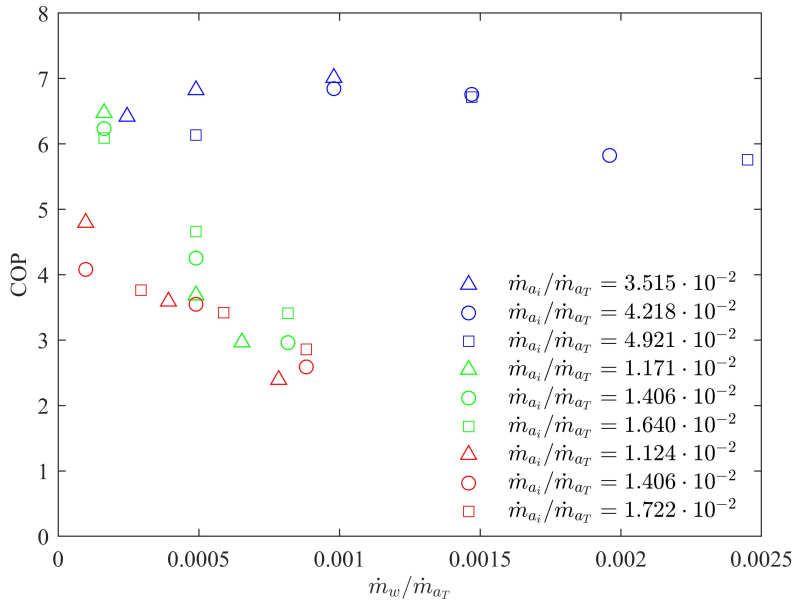

Figure 13. Coefficient of performance as a function of the water-to-air mass flow ratio for all the simulations conducted.

4. Conclusions

In this paper, a numerical model of an ultrasonic mist generator for the evaporative pre-cooling of the inlet air of the condenser in air conditioning applications has been developed. Several experimental test runs were conducted in an experimental facility specifically adapted for that purpose to validate the results predicted by the model. Afterwards, a parametric analysis including some physical variables involved in the cooling process was carried out. Finally, an optimization study regarding the overall cooling performance of the ultrasonic generator, for the above mentioned application, was performed. The main conclusions obtained during this investigation can be summarized as follows.

- The average evaporative cooling efficiency evaluated at the outlet section of the domain, $\bar{\eta}^L$, increases when the water-to-air mass flow and air-to-air mass flow ratios ($\dot{m}_w/\dot{m}_{a_T}$ and $\dot{m}_{a_i}/\dot{m}_{a_T}$) increase. A maximum value of $\bar{\eta}^L = 0.654$ is found for $\dot{m}_w/\dot{m}_{a_T} = 0.00244$ and $\dot{m}_{a_i}/\dot{m}_{a_T} = 0.0492$.
- A dimensionless correlation for the average evaporative cooling efficiency evaluated at the outlet section of the domain, $\bar{\eta}^L$, as a function of the relevant parameters has been developed. It shows an excellent agreement with the predicted results.
- The observations regarding the wet length have allowed identifying the operation ranges that produce a more homogeneous distribution of water mist and, therefore, promote the evaporation. These ranges are $2.5 \times 10^{-4} \leq \dot{m}_w/\dot{m}_{a_T} \leq 0.002$ and $0.035 \leq \dot{m}_{a_i}/\dot{m}_{a_T} \leq 0.05$.
- The optimization analysis based on the coefficient of performance has proven that the operational ranges leading to the best overall performance are $5 \times 10^{-4} \leq \dot{m}_w/\dot{m}_{a_T} \leq 0.002$ and

$0.035 \leq \dot{m}_{a_i} / \dot{m}_{a_T} \leq 0.05$. Under these conditions, there is a better distribution of the water mist throughout the control section and a more homogeneous and effective evaporative cooling process. This will not only improve the performance of the air-cooled condenser heat pump, but also lower the overall ancillary power consumption.

Author Contributions: Conceptualization, J.R. and M.L.; methodology, J.R., P.M. and M.L.; software, J.R., Í.M. and P.M.; validation, J.R., P.M. and Í.M.; formal analysis, J.R., P.M. and Í.M.; investigation, J.R. and Í.M.; resources, J.R. and M.L.; data curation, J.R. and P.M.; writing—original draft preparation, J.R., P.M. and Í.M.; writing—review and editing, J.R., P.M. and M.L.; visualization, J.R., P.M. and M.L.; supervision, M.L.; project administration, M.L.; and funding acquisition, M.L. All authors have read and agreed to the published version of the manuscript.

Funding: This research was funded by FEDER/Ministerio de Ciencia e Innovación–Agencia Estatal de Investigación throuhg Spanish research projects ENE2017-83729-C3-1-R and ENE2017-83729-C3-3-R, supplied by FEDER funds.

Conflicts of Interest: The authors declare no conflict of interest. The funders had no role in the design of the study; in the collection, analyses, or interpretation of data; in the writing of the manuscript, or in the decision to publish the results.

Abbreviations

The following abbreviations are used in this manuscript:

Symbols

A_d	area of the droplet (m^2)
A_T^x	percentage area for temperature T, at section x (-)
b	domain width (m)
C_D	drag coefficient (-)
c_p	specific heat at constant pressure (J kg^{-1} K^{-1})
D	mist inlet area diameter (m)
D_f	mass diffusivity (m^2 s^{-1})
d_d	droplet diameter (m)
d_{10}	arithmetic mean diameter (m)
d_{32}	Sauter mean diameter (m)
$\bar{d}$	Rosin–Rammler mean drop diameter (m)
Δp	pressure loss (Pa)
F_c	safety factor numerical value in the GCI analysis ($F_c = 3$) (-)
g	gravitational constant (m s^{-2})
h	domain height (m)
h_C	heat transfer coefficient (W m^{-2} K^{-1})
h_D	mass transfer coefficient (m s^{-1})
h_{fg}	enthalpy of vaporization (J kg_w^{-1})
L	domain length (m)
L_w	wet length (m)
l	distance between inlet sections (m)
M	cumulative mass fraction (-)
m	mass (kg)
$\dot{m}_{a_i}$	air mass flow rate at the mist discharge section (kg s^{-1})
$\dot{m}_{a_T}$	air mass flow rate at the inlet section of the domain (kg s^{-1})
$\dot{m}_w$	mass flow rate of water mist (kg_w s^{-1})
Nu	Nusselt number (-)
N	number of droplets (-)
n	Rosin–Rammler spread factor (-)
p	pressure (Pa)
Pr	Prandtl number (-)

Q	volumetric flow rate of air ($m^3\ s^{-1}$)
$\dot{Q}_{cooling}$	cooling capacity (W)
Re	Reynolds number (-)
r	grid refinement ratio in the GCI analysis (-)
Sc	Schmidt number (-)
Sh	Sherwood number (-)
s	order of convergence in the GCI analysis ($s = 2$) (-)
T	dry temperature (°C)
T_{wb}	wet bulb temperature (°C)
T_{wi}	temperature of the water in the tank (°C)
$\bar{T}^x$	mean temperature calculated at section x (°C)
t	time (s)
v_i	average air flow velocity in the mist discharge section ($m\ s^{-1}$)
v_T	average air flow velocity in the wind tunnel ($m\ s^{-1}$)
$\dot{W}_{fan_T}$	power absorbed by the primary fan (W)
$\dot{W}_{fan_i}$	power absorbed by the secondary fan (W)
$\dot{W}_{ultrasound}$	power absorbed ultrasonic generator device (W)
y	molar concentration ($mol\ m^{-3}$)

Greek symbols

ε	relative error of the solutions in the GCI analysis (-)
η_f	fan efficiency (-)
$\bar{\eta}^x$	evaporative cooling efficiency calculated at section x (-)
μ	dynamic viscosity ($kg\ m^{-1}\ s^{-1}$)
ω	mass fraction of moist air ($kg_w\ kg_{ma}^{-1}$)
ϕ	relative humidity (-)
ρ	density ($kg\ m^{-3}$)
τ	stress tensor ($kg\ m^{-3}$)
Re	Reynolds number (-)

Subscripts

a	air
d	droplet
∞	ambient conditions
ma	moist air
w	water

Abbreviations

CFD	computational fluid dynamics
COP	coefficient of performance
GCI	grid convergence index
HVAC	heating, ventilation and air-conditioning
SMD	Sauter mean diameter

References

1. IEA. *The Future of Cooling: Opportunities for Energy-Efficient Air Conditioning*; Annual report; IEA: Paris, France, 2018.
2. Martínez, P.; Ruiz, J.; Cutillas, C.; Martínez, P.; Kaiser, A.; Lucas, M. Experimental study on energy performance of a split air-conditioner by using variable thickness evaporative cooling pads coupled to the condenser. *Appl. Therm. Eng.* **2016**, *105*, 1041–1050. [CrossRef]
3. Ibrahim, N.I.; Al-Farayedhi, A.A.; Gandhidasan, P. Experimental investigation of a vapor compression system with condenser air pre-cooling by condensate. *Appl. Therm. Eng.* **2017**, *110*, 1255–1263. [CrossRef]
4. Yu, F.; Ho, W.; Chan, K.; Sit, R. Theoretical and experimental analyses of mist precooling for an air-cooled chiller. *Appl. Therm. Eng.* **2018**, *130*, 112–119. [CrossRef]
5. Hooman, K.; Guan, Z.; Gurgenci, H. 9-Advances in dry cooling for concentrating solar thermal (CST) power plants. In *Advances in Concentrating Solar Thermal Research and Technology*; Blanco, M.J., Santigosa, L.R.,

Eds.; Woodhead Publishing Series in Energy, Woodhead Publishing: Cambridge, UK, 2017; pp. 179–212. [CrossRef]
6. Yao, Y. Research and applications of ultrasound in HVAC field: A review. *Renew. Sustain. Energy Rev.* **2016**, *58*, 52–68. [CrossRef]
7. Yao, Y.; Pan, Y.; Liu, S. Power ultrasound and its applications: A state-of-the-art review. *Ultrason. Sonochemistry* **2020**, *62*, 104722. [CrossRef] [PubMed]
8. Tissot, J.; Boulet, P.; Trinquet, F.; Fournaison, L.; Macchi-Tejeda, H. Air cooling by evaporating droplets in the upward flow of a condenser. *Int. J. Therm. Sci.* **2011**, *50*, 2122–2131. [CrossRef]
9. Hou, Y.; Tao, Y.; Huai, X.; Guo, Z. Numerical characterization of multi-nozzle spray cooling. *Appl. Therm. Eng.* **2012**, *39*, 163–170. [CrossRef]
10. Alkhedhair, A.; Gurgenci, H.; Jahn, I.; Guan, Z.; He, S. Numerical simulation of water spray for pre-cooling of inlet air in natural draft dry cooling towers. *Appl. Therm. Eng.* **2013**, *61*, 416–424. [CrossRef]
11. Xia, L.; Gurgenci, H.; Liu, D.; Guan, Z.; Zhou, L.; Wang, P. CFD analysis of pre-cooling water spray system in natural draft dry cooling towers. *Appl. Therm. Eng.* **2016**, *105*, 1051–1060. [CrossRef]
12. Sadafi, M.; Ruiz, J.; Lucas, M.; Jahn, I.; Hooman, K. Numerical and experimental study on a single cone saline water spray in a wind tunnel. *Int. J. Therm. Sci.* **2017**, *120*, 190–202. [CrossRef]
13. Kim, K.D.; Jin, D.H.; Choi, Y.C. Numerical simulation on the generation of ultrasound and formation of water fog in the ultrasonic gas atomizer. *Ultrasonics* **2020**, *102*, 105851. [CrossRef] [PubMed]
14. Ruiz, J. Experimental Characterization and Modelling of the Binomial Distribution System-Drift Eliminator in Cooling Towers. Ph.D. Thesis, Technical University of Cartagena, Cartagena, Spain, 2014.
15. Martínez, P.; Ruiz, J.; Martínez, P.; Kaiser, A.; Lucas, M. Experimental study of the energy and exergy performance of a plastic mesh evaporative pad used in air conditioning applications. *Appl. Therm. Eng.* **2018**, *138*, 675–685. [CrossRef]
16. Ruiz, J.; Cutillas, C.; Kaiser, A.; Zamora, B.; Sadafi, H.; Lucas, M. Experimental study on pressure loss and collection efficiency of drift eliminators. *Appl. Therm. Eng.* **2019**, *149*, 94–104. [CrossRef]
17. Meroney, R.N. CFD prediction of cooling tower drift. *J. Wind Eng. Ind. Aerodyn.* **2006**, *94*, 463–490. [CrossRef]
18. Lucas, M.; Martínez, P.; Ruiz, J.; Kaiser, A.; Viedma, A. On the influence of psychrometric ambient conditions on cooling tower drift deposition. *Int. J. Heat Mass Transf.* **2010**, *53*, 594–604. [CrossRef]
19. Montazeri, H.; Blocken, B.; Hensen, J. Evaporative cooling by water spray systems: CFD simulation, experimental validation and sensitivity analysis. *Build. Environ.* **2015**, *83*, 129–141. doi:10.1016/j.buildenv.2014.03.022. [CrossRef]
20. Sadafi, M.; Jahn, I.; Hooman, K. Nozzle arrangement effect on cooling performance of saline water spray cooling. *Appl. Therm. Eng.* **2016**, *105*, 1061–1066. [CrossRef]
21. Alkhedhair, A.; Jahn, I.; Gurgenci, H.; Guan, Z.; He, S.; Lu, Y. Numerical simulation of water spray in natural draft dry cooling towers with a new nozzle representation approach. *Appl. Therm. Eng.* **2016**, *98*, 924–935. [CrossRef]
22. Zhang, Z.; He, S.; Yan, M.; Gao, M.; Shi, Y.; Lu, Y.; Liu, J.; Guo, C.; Huang, X. Numerical study on the performance of a two-nozzle spray cooling system under different conditions. *Int. J. Therm. Sci.* **2020**, *152*, 106291. [CrossRef]
23. Morsi, S.A.; Alexander, A.J. An investigation of particle trajectories in two-phase flow systems. *J. Fluid Mech.* **1972**, *55*, 193–208. [CrossRef]
24. Ranz, W.E.; Marshall, W.R. Evaporation from drops part I. *Chem. Eng. Prog.* **1952**, *48*, 141–146.
25. Ranz, W.E.; Marshall, W.R. Evaporation from drops part II. *Chem. Eng. Prog.* **1952**, *48*, 173–180.
26. Ruiz, J.; Kaiser, A.; Zamora, B.; Cutillas, C.; Lucas, M. CFD analysis of drift eliminators using RANS and LES turbulent models. *Appl. Therm. Eng.* **2016**, *105*, 979–987. [CrossRef]
27. ANSYS FLUENT ©Academic Research, ANSYS FLUENT 19. 2018. Available online: https://www.ansys.com (accessed on 1 February 2019).
28. Roache, P.J. *Computational Fluid Dynamics*; Hermosa Publishers: Albuquerque, NM, USA, 1972; p. 446.